Article

Modeling and Analysis of Mass Transport Losses of Proton Exchange Membrane Water Electrolyzer

Tamara Miličić [1,*], **Haashir Altaf [2]**, **Nicole Vorhauer-Huget [2]**, **Luka A. Živković [1]**, **Evangelos Tsotsas [2]** and **Tanja Vidaković-Koch [1]**

[1] Electrochemical Energy Conversion, Max Planck Institute for Dynamics of Complex Technical Systems, Sandtorstrasse 1, 39106 Magdeburg, Germany

[2] Thermal Process Engineering, Otto von Guericke University, Universitaetsplatz 2, 39106 Magdeburg, Germany

* Correspondence: milicic@mpi-magdeburg.mpg.de; Tel.: +49-391-675-7634

Abstract: Proton exchange membrane water electrolyzers (PEMWEs) coupled with renewable energy resources are considered to be a key technology for producing green hydrogen. However, the high current density PEMWE operation features remarkable voltage losses. A significant part of these losses is due to the mass transport resistance in the PEMWE. Even though the importance of mass transport resistance is widely recognized, it is still poorly understood. Currently, the two-phase transport through the anode porous transport layer (PTL) and catalyst layer is considered to be the main cause of the mass transport losses. In this work, a dynamic macroscopic mathematical model, coupling electrochemical reaction with mass transport through the PTL and flow channels, has been developed to study the two-phase flow in the PTL and mass transport losses of a PEMWE. The influence of the current density, inlet water flow rate, PTL structural parameters, and capillary pressure curve was evaluated. The existence of the critical current density was observed, as well as its dependence on the operating parameters and PTL structure. Even though the results show that the PTL structure has a significant influence on the PEMWE performance, they indicate that a better mathematical description of the two-phase flow in the PTL is necessary.

1. Introduction

Concerns about climate change, air quality, and the stability of the energy supply have stimulated an energy transition toward renewable and clean sources. The major drawback of the primary renewable energy resources is their intermittency. To overcome the longer-term energy disruptions and, on the other hand, to prevent energy dissipation during excess generation, efficient energy storage is needed [1,2]. Due to its high dynamic range, high efficiencies, and the high purity of the produced gases [3], a proton exchange membrane water electrolyzer (PEMWE) is considered to be a key technology for tackling this issue. However, this technology faces many challenges [4]. Producing large quantities of hydrogen requires operation at a high current density. Yet, when operated at high current densities, high potential losses occur. The increase in cell voltage with the current density has been observed in many works and can be ascribed to different phenomena. One of the causes of the high potential losses is the transport resistance through the porous transport layer (PTL) of the anode compartment of the electrolyzer.

A PTL is a porous structure on the anode of the PEMWE that, on the one hand, serves as a current collector for conducting electrons from the anode catalyst layer (ACL) to the flow field and, on the other hand, for the supply of water and the removal of the produced oxygen from the ACL [4]. Additionally, it provides a mechanical stability to the membrane electrode assembly (MEA) and facilitates the heat removal from the catalyst layer to the

flow fields. Thus, the PTL needs to have a high electrical and thermal conductivity; to be chemically stable in the anodic environment of the PEMWE (a low pH, presence of oxygen, and relatively high potential); to facilitate the transport of water for a reaction and produced oxygen; to provide good contact to the ACL and flow field; to be mechanically stable, especially under a pressurized operation; and to be economically viable for a large-scale application [5]. Satisfying all of the mentioned requirements proved to be challenging.

State-of-the-art PTLs are made of titanium fibers or powder. Titanium is mechanically and chemically stable in the anodic environment of the PEMWE and has good electrical and thermal conductivity. However, it passivates over time, forming a thin non-conductive layer on the surface. For this reason, it is usually coated with platinum-group metals. Furthermore, the counter-current transport of water and oxygen through the PTL is considered to be critical, leading to the accumulation of gas in both the PTL and the ACL, and a hindrance to the water supply. This results in mass transport overpotential. Several studies have focused on the influence of the operating conditions on mass transport losses [6–9]. It has been shown that the PTL structure can have a detrimental effect on mass transport and its influence on the electrolyzer performance has been studied extensively. Peng et al. [10] found that the PTL bulk porosity and tortuosity have a considerable impact on the mass transport losses because they determine the liquid and gas transport across the PTL. An optimal pore size for minimizing the mass transport losses has been proposed [11,12], while less porous PTLs showed an increase in mass transport losses [13].

Furthermore, recent studies have shown that the interface between the PTL and ACL has a dominant influence on the electrolyzer performance compared to the bulk of the PTL [12,14–16]. Large pores at the PTL interface cause poor contact between the catalyst nanoparticles and the PTL material. Schuler et al. [16] showed that this results in a higher ohmic contact resistance, lower ACL utilization, and local mass transport resistance through the ionomer and its interfaces. To overcome this problem, in their next publication, they have suggested the utilization of hierarchically structured PTLs: commercial PTLs with different microporous layers (MPLs) showed a better performance due to the better ACL utilization [17]. Similar findings were obtained from the PEMWE operando neutron imaging study presented in [18]. Alternatively, Mo et al. [19] have proposed the utilization of a planar titanium PTL with straight-through pores, a so-called thin–tunable, liquid–gas diffusion layer. To reduce the interfacial contact resistance, different surface treatment methods, as well as titanium micro- and nanoporous layers were investigated [20,21]. The obtained PTLs showed a better performance compared to the state-of-the-art PTLs.

Although many studies show that the PTLs have an influence on the electrolyzer performance, the impact is difficult to quantify in terms of the potential loss due to mass transport. In most studies, a simplified approach has been adopted where it was assumed that all the deviations from the Tafel behavior at higher current densities can be ascribed to mass transport losses [6,10,15–17,22]. Based on this approach, mass transport losses ranging from a few to 100 or even 1000 mV have been estimated. More insights into the mass transport losses and their dependence on the PTL structure can be gained with the help of mathematical models. In this respect, despite their averaging character, macroscale models appear to be highly suitable, because they can calculate the overall electrolyzer performance at a low computational cost. Many models have been developed to describe the electrochemical behavior of the PEMWE [23], but only a few consider the influence of the two-phase flow in the anode PTL.

Schmidt et al. [24] developed a multiphase continuum model for the flow in the PTL, including the Darcian flow and advective–diffusive mass transport. This model was able to simulate the influence of the operating parameters on the mass transport overpotential, with an overestimation at low current densities. However, the influence of the PTL material properties was not in agreement with the experimental results. One of the rare dynamic PEMWE models is presented in [25]. A 1D model for the mass and energy transport along the flow channels was coupled with the water transport through the membrane, gas crossover, and electrochemical kinetics. The model was used to analyze the performance

of the cell stack at different operating conditions. Han et al. [26] used the porous media flow theory for the evaluation of the steady-state PEMWE operation. The model was able to simulate experimentally obtained polarization curves and was used for investigating the effects of the contact angle, PTL porosity, and PTL thickness on the liquid saturation, voltage, and efficiency of a PEMWE. The influence of the flow rate on mass transport in the PTL was not shown. A steady-state, 1D, multiphase, nonisothermal model of the PEMWE incorporating the mass, momentum, gas species, charge and energy conservation equations across the membrane, catalyst layers, and PTLs was introduced in [27]. A good agreement with the experimental polarization curves from the literature was achieved and a parameter sensitivity analysis was performed. Wrubel et al. [28] developed a 2D steady-state PEMWE model that coupled the electrochemistry and charge transport in the membrane and catalyst layers with the multiphase mass transport in the catalyst layers and PTLs. It was used for studying novel anode PTLs (thin–tunable, liquid–gas diffusion layers) and has not been yet applied to the state-of-the-art PTLs.

In this work, a macroscopic dynamic model has been developed to quantify the mass transport losses and analyze the electrolyzer performance. The model assumes that the mass transport losses can be assigned to the slow two-phase transport in the anode PTL, which then causes the gas produced to accumulate in the ACL. Thus, the active electrode area for the electrochemical reaction is reduced.

2. Mathematical Model

The PEMWE schematic considered for the model development is shown in Figure 1. The electrolyzer is separated into four domains: anode flow channel (AFC), PTL, membrane electrode assembly (MEA, containing membrane, MEM, and catalyst layers; ACL and cathode catalyst layer (CCL)), and cathode (C). The influence of two-phase transport in the gas diffusion layer (GDL) of the cathode compartment of the electrolyzer is not taken into consideration in this model, and transport through the PTL is considered to be the only source of mass transport overpotential. Each domain is modeled individually and coupled with other domains through the use of appropriate boundary conditions. Two-phase flow in the PTL, AFC, and C is considered, taking into account water evaporation and condensation. Gases in the system are assumed to behave ideally. Crossover of gases through the membrane is disregarded (only atmospheric pressure operation was considered), as is their dissolution in water (solubility of oxygen and hydrogen is low under the operating conditions considered). Isothermal, isobaric operation is assumed and spatial distribution across the active area has been disregarded. These assumptions are more valid for smaller electrolysis cells and higher inlet flow rates. The model takes into account the transient behavior of the PEMWE due to the dynamics of charge transfer reaction and mass transport in the flow channels and PTL.
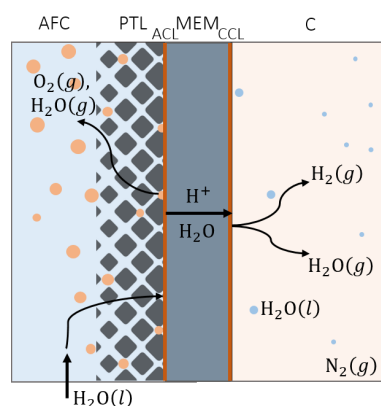
Figure 1. Schematic representation of the PEMWE: AFC—anode flow channel, PTL—anode porous transport layer, ACL—anode catalyst layer, MEM—membrane, CCL—cathode catalyst layer, C—cathode flow channel, *g*—gas, *l*—liquid.

2.1. Flow Channel Model

The mass balance of species in the AFC is derived assuming the ideal mixing of the species:

$$\frac{dC_i^{AFC}(t)}{dt} = \frac{U_{A,0}C_{i,0}^{AFC}}{l} - \frac{U_A C_i^{AFC}}{l} + \psi_i^{AFC}(t) \qquad i = H_2O(l), H_2O(g), O_2(g) \quad (1)$$

where C_i represents the molar concentration of species i, U is flow velocity, l is the length of the flow channels, and index 0 marks the value at the inlet. The liquid and gas velocities are assumed to be equal and calculated based on the conservation of the total volume of the gas–liquid mixture which flows through the channels, as described in [25]. The term $\psi_i^{AFC}(t)$ represents sinks and sources of mass due to the transport between AFC/PTL, and water-phase change.

The mass balance of the C is derived with the same assumptions as for the AFC, i.e., ideal mixing and equal velocities of gas and liquid phases:

$$\frac{dC_i^{C}(t)}{dt} = \frac{U_{C,0}C_{i,0}^{C}}{l} - \frac{U_C C_i^{C}}{l} + \psi_i^{C}(t) \qquad i = H_2O(l), H_2O(g), H_2(g), N_2(g) \quad (2)$$

The sources and sinks term $\psi_i^{C}(t)$ stands for the water phase change and reaction rate of hydrogen evolution reaction.

The molar concentrations in Equations (1) and (2) are expressed as the number of moles in the total volume of the gas–liquid mixture.

The water-phase-change flux is determined based on the rate constant, k_w, and driving force: the difference between partial pressure of the water in the vapor–oxygen (vapor-hydrogen-nitrogen) mixture, $p_{H_2O}^{I}$, and vapor pressure, $p_{H_2O}^{sat}$:

$$R_w^{I} = k_w \frac{\epsilon_I(t)}{RT} \left(p_{H_2O}^{I}(t) - p_{H_2O}^{sat} \right) \qquad I = AFC, C \quad (3)$$

where ϵ is the volume fraction of gas in the two-phase mixture. The vapor pressure at cell operating temperature was determined using the Antoine equation [29].

2.2. Anode Porous Transport-Layer Model

The PTL is modeled based on the multiphase flow model [30]. The spatial distribution in the direction perpendicular to the membrane, z, is considered. The following equations describe two-phase transport in the PTL:

$$\varepsilon(z)\frac{\partial(\rho_k(t,z)s_k(t,z))}{\partial t} + \frac{\partial(\rho_k(t,z)u_k(t,z))}{\partial z} = \psi_k(t,z) \qquad k = l, g \qquad \psi_{l,g} = \pm R_w M_{H_2O} \quad (4)$$

$$\varepsilon(z)\frac{\partial(\rho_g(t,z)s_g(t,z)y_i^{PTL}(t,z))}{\partial t} +$$
$$\frac{\partial}{\partial z}\left(\rho_g(t,z)u_g(t,z)y_i^{PTL}(t,z) - \varepsilon(z)\rho_g(t,z)s_g(t,z)D_i^{eff}(z)\frac{\partial y_i^{PTL}(t,z)}{\partial z} \right) = \psi_i(t,z) \quad (5)$$
$$i = H_2O(g), O_2(g)$$

In these equations, $\varepsilon(z)$ is the porosity of the PTL, ρ_k is phase k density, s_k is phase k saturation, and y_i is the molar fraction of the component i in the gas phase. The liquid phase was considered to be incompressible. Bruggeman's equation was used for determining effective diffusivities of species:

$$D_i^{eff}(z) = D_{ij}\frac{\varepsilon(z)}{\tau(z)} \quad (6)$$

where D_{ij} is the diffusion coefficient and τ is the tortuosity of the PTL.

Capillary pressure in porous media correlates the pressure of gas with the liquid pressure. It can be determined based on saturation and PTL properties [30]. The Leverette capillary pressure curve is widely used for calculating capillary pressure in electrolyzer modeling [26,31]:

$$p_c(t,z) = p_g(t,z) - p_l(t,z) = \sigma cos(\gamma)\left(\frac{\varepsilon(z)}{K}\right)^{0.5} J(S(t,z)) \tag{7}$$

where σ is the surface tension, γ is the contact angle, and K is the absolute permeability of the porous medium. $J(S(t,z))$ is the Leverette function that introduces the capillary pressure dependence on saturation.

$$J(S) = \begin{cases} 1.417(1 - S(t,z)) - 2.120(1 - S(t,z))^2 + 1.263(1 - S(t,z))^3, & 0° < \gamma < 90° \\ 1.417S(t,z) - 2.120S(t,z)^2 + 1.263S(t,z)^3, & 90° < \gamma < 180° \end{cases} \tag{8}$$

The Brooks–Corey correlation is one of the alternatives for calculating capillary pressure [32]. The following formulation has been proposed for its application in fuel cell and electrolyzer modeling [33]:

$$p_c(t,z) = p_g(t,z) - p_l(t,z) = \frac{2\sigma cos(\gamma)}{r_{max}} S(t,z)^{\frac{1}{\lambda}} \tag{9}$$

where r_{max} is the largest pore diameter and λ is the pore size distribution (PSD) index. The greater the value of the PSD index, the narrower the PSD, with most pores being close to the size of the largest pore [33].

$S(t,z)$ in Equations (7)–(9) is normalized liquid saturation, taking into account the residual saturation, s_r, which states that part of the PTL is inactive for the two-phase transport:

$$S(t,z) = \frac{s(t,z) - s_r}{1 - s_r} \tag{10}$$

Residual saturation was considered to be constant with regard to time and space.

Figure 2 shows the dependency of capillary pressure on the liquid saturation calculated with the Leverette equation (LE) and Brooks–Corey equation (BCE). The influence of porosity on LE capillary pressure, as well as the influence of the maximal pore radius and the PSD index on BCE capillary pressure is also presented. The PSD index is a fitting parameter in the BCE. A large discrepancy between the LE and BCE capillary pressure curves is evident, especially at the lower saturation values. Furthermore, the capillary pressure curve based on the BCE shows a high degree of sensitivity to maximal pore radius, and even greater sensitivity to the PSD index. A pore network model (PNM) study showed that the invasion patterns of the PTL, and thus PTL liquid saturation, are more sensitive to PSD than to porosity [34]. This effect of PSD is taken into account when describing capillary pressure using the BCE. Equations (7) and (9) are compared and evaluated for the PEMWE application in this work.

Except for capillary pressure correlations, such as LE and BCE that were used here, there were few attempts to calculate capillary pressure curves based on the PTL structure. Lettenmeier et al. [35] determined capillary pressure curves of studied PTLs by applying the pore-morphology method that is implemented in the GeoDict commercial software program. On the other hand, Stieber et al. [36] used PNM simulations to determine the PTL capillary pressure curve. Capillary pressure curves in [35,36] showed behavior between those obtained with LE and BCE: at lower saturations, they behaved in the same way as the BCE curves, while at higher saturations, they were similar to the LE curve.

The phase velocity is calculated based on generalized Darcy's law, with the effect of gravity being disregarded:

$$u_k(t,z) = -K \frac{k_{r,k}(t,z)}{\mu_k(t,z)} \frac{\partial p_k(t,z)}{\partial z} \tag{11}$$

Relative permeability, $k_{r,k}$, is a function of phase saturation. Usually, the exponential form is used:

$$k_{r,k}(t,z) = S_k(t,z)^n \tag{12}$$

with exponent n being equal to 3 [26,31,33]. This form was used for the calculations with LE. However, the BCE model uses different expressions to calculate the relative permeabilities [33]:

$$k_{r,l}(t,z) = S(t,z)^{\frac{2+3\lambda}{\lambda}} \qquad k_{r,g}(t,z) = (1 - S(t,z))^2 S(t,z)^{\frac{2+\lambda}{\lambda}} \tag{13}$$

The sink and source term in the PTL mass conservation balances (4) and (5) represents the phase change of water, with the rate of evaporation/condensation in the PTL calculated as:

$$R_w^{\text{PTL}} = \frac{k_w \varepsilon(z)(1 - s_l(t,z))}{RT} \left(y_{\text{H}_2\text{O}}^{\text{PTL}}(t,z) p_g(t,z) - p_{\text{H}_2\text{O}}^{sat} \right) \tag{14}$$
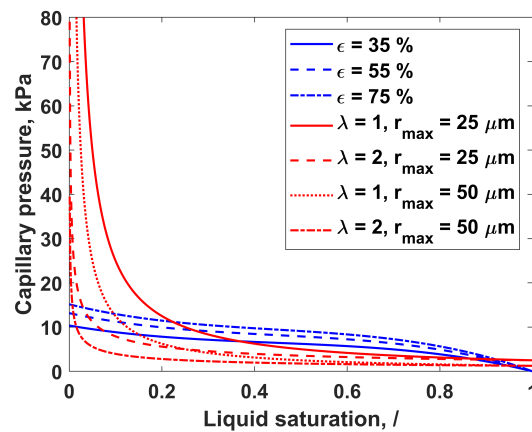
Figure 2. Capillary pressure as a function of the liquid saturation calculated with LE for different porosities, ε (blue lines) and with BCE for different PSD indices, λ (red lines).

2.3. Membrane Model

The membrane is considered impermeable for the gaseous species. Only the protons and liquid water are transported through the membrane. The water flux through the membrane is determined as a sum of flux due to the concentration gradient between the anode and cathode compartments, and flux due to electro-osmotic drag:

$$N_{\text{H}_2\text{O}}^{mem}(t) = N_{\text{H}_2\text{O}}^{diff}(t) + N_{\text{H}_2\text{O}}^{eod}(t) = \frac{D_w}{h_{mem}} \left(C_{\text{H}_2\text{O}}^{\text{ACL}}(t) - C_{\text{H}_2\text{O}}^{\text{ACL}}(t) \right) + n_{eod} \frac{j}{F} \tag{15}$$

where n_{eod} is the electro-osmotic drag coefficient and j is the current density.

2.4. Cell Voltage Model

The cell voltage is calculated as the sum of the open-circuit voltage and cell overpotentials:

$$E_{cell}(t) = E_{ocv} - \eta_{\text{A}}(t) - |\eta_{\text{C}}(t)| - \eta_{ohm}(t) \tag{16}$$

The open-circuit voltage is determined based on the Gibbs free energy ΔG of the reaction as a function of temperature and pressure. The effect of the concentration changes is disregarder:

$$E_{ocv} = -\frac{\Delta G(T, p)}{nF} \tag{17}$$

The total cell overpotential is represented by three individual overpotentials: anode kinetic overpotential, cathode kinetic overpotential, and ohmic overpotential. The biggest contributor to the ohmic losses of the cell is assumed to be the proton conduction through the membrane. Only membrane resistance is taken into account for calculating ohmic overpotential:

$$\eta_{ohm} = \frac{h_{mem}}{\kappa_{mem}} j(t) \tag{18}$$

where h_{mem} is the membrane thickness and κ_{mem} is membrane conductivity. The conductivity of the Nafion membrane is calculated as a function of the temperature and humidity λ_{mem} [25], assuming that the membrane is fully humidified:

$$\kappa_{mem} = (0.005139\lambda_{mem} - 0.00326) exp\left[1268\left(\frac{1}{303} - \frac{1}{T}\right)\right] \quad \mathrm{S\,cm^{-1}} \tag{19}$$

Anode and cathode kinetic overpotentials are determined from the charge balances:

$$C_{dl}^{A} \frac{d\eta_{A}(t)}{dt} = (j(t) - 4Fr_{A}(t)) \tag{20}$$

$$C_{dl}^{C} \frac{d\eta_{C}(t)}{dt} = (-j(t) + 2Fr_{C}(t)) \tag{21}$$

where C_{dl} is a double-layer capacity. The mass transport resistance is included in the η_{A} term together with the kinetic resistance. Oxygen evolution reaction is not limited by mass transport due to the decrease in reactant concentration, as water is always present in surplus. Instead, the limitation is expressed by the slow removal of the reaction product (oxygen gas). To account for this, two approaches are considered in the literature. In one approach, the accumulation of oxygen gas at the ACL/PTL interface is accounted for by changing the equilibrium potential of the oxygen evolution reaction (Nernst equation) [25,37,38]. In another approach, the oxygen gas is assumed to block part of the electrode surface, which increases the overall overpotential of the anode [26–28]. In the present work, we followed the latter approach and considered part of the anode to be covered with gas bubbles and therefore inactive for electrochemical oxidation of water. To take this into account, a parameter representing the part of the electrode area covered with bubbles (θ) is introduced into the classical form of the Tafel equation. This parameter is called bubble coverage, and it is assumed to be equal to the gas saturation at the ACL/PTL interface. The reaction rate at the anode is then written as follows:

$$r_{A}(t) = \frac{j_{0,A}}{4F}(1 - \theta(t))\exp\left(\frac{\alpha_{A}F}{RT}\eta_{A}\right) \tag{22}$$

where α is the charge transfer coefficient and i_0 is the exchange current density. Thus, the overpotential of the anode includes both activation overpotential and mass transfer overpotential. The saturation at the interface is dependent on both the PTL structure and the flow conditions in the channel.

For the cathode, mass transfer limitations are considered negligible (cathode overpotential is equal to the activation overpotential) and the Butler–Volmer equation is used to calculate the reaction rate:

$$r_{C}(t) = \frac{j_{0,C}}{2F}\sinh\left(-\frac{\alpha_{C}F}{RT}\eta_{C}\right) \tag{23}$$

The dynamics of the electrochemical process are described by Equations (20)–(23).

3. Results and Discussion

The obtained model is a differential-algebraic (DAE) system, with nine ordinary differential Equations (1), (2), (20), and (21) and three partial differential Equations (4) and (5). For solving this system, the discretization of the partial differential equations was performed using the finite volume method. The following boundary conditions were used:

- The Dirichlet boundary condition at the AFC/PTL interface (the gas pressure, liquid saturation, and oxygen molar fraction are the same as in the bulk of the AFC);
- The Neumann boundary condition at the ACL/ PTL interface (the equality of the fluxes on the ACL and PTL side of the boundary).

All the boundary conditions are summarized in Table 1.

Table 1. Boundary conditions for partial differential equations of the PTL model.

AFC/PTL Interface	
$p_l\vert_{\text{AFC}} = p$	(24)
$s_l\vert_{\text{AFC}} = 1 - \epsilon$	(25)
ACL/PTL Interface	

$$-\left(\rho_g y_{\text{O}_2}^{\text{PTL}} K \frac{K_{r,g}^{\text{PTL}}}{\mu_g} \frac{\partial p_g}{\partial z}\right)\bigg|_{\text{ACL}} - \left(\varepsilon\rho_g(1-s_l)D_{\text{O}_2}^{eff} \frac{\partial y_{\text{O}_2}^{\text{PTL}}}{\partial z}\right)\bigg|_{\text{ACL}} = -r_{\text{A}}M_{\text{O}_2} \qquad (26)$$

$$-\rho_{\text{H}_2\text{O}}\left(K \frac{K_{r,l}^{\text{PTL}}}{\mu_l} \frac{\partial p_l}{\partial z}\right)\bigg|_{\text{ACL}} = \left(2r_{\text{A}} + N_{\text{H}_2\text{O}}^{mem}\right)M_{\text{H}_2\text{O}} \qquad (27)$$

$$-\left(\rho_g y_{\text{H}_2\text{O},g}^{\text{PTL}} K \frac{K_{r,g}^{\text{PTL}}}{\mu_g} \frac{\partial p_g}{\partial z}\right)\bigg|_{\text{ACL}} - \left(\varepsilon\rho_g(1-s_l)D_{\text{H}_2\text{O}}^{eff} \frac{\partial y_{\text{H}_2\text{O},g}^{\text{PTL}}}{\partial z}\right)\bigg|_{\text{ACL}} = 0 \qquad (28)$$

Based on the analysis of the sensitivity of the profiles through the PTL, 50 elements were chosen for the discretization. The obtained DAE system was used for the dynamic simulations in Matlab. The model parameters are shown in Table S1 of Supplementary Information. The influence of the operating parameters (the current density and inlet water flow rate) was investigated by changing the analyzed parameter and keeping the rest constant. The parameters of the LE and BCE capillary pressure curves were set following the structural data of the PTLs analyzed in [15,39], as shown in Table 2.

Table 2. PTL parameters.

Parameter	PTL1	PTL2	PTL3	PTL4	PTL5
Porosity, ε, %	35 *	55 *	54 *	57 *	75 *
Mean fiber diameter, d_{mean}, µm	52 *	11 *	15.4 *	30.1 *	11.1 *
Maximum pore radius, r_{max}, µm	25	35 *	43 *	70 *	50 *
Tortuosity, τ, /	1.6 *	1.6 *	1.6 *	1.3 *	1.2 *
Absolute permeability, K, m^2	3.4×10^{-12} *	2.2×10^{-12} *	3.3×10^{-12} *	2.69×10^{-11} *	1.94×10^{-11} *
PSD index, λ, /	2	2	1.9	1	1.5

* Adopted from [15,39].

### 3.1. Influence of Operating Conditions

The influence of the operating current density and inlet water flow rate were studied by analyzing the performance at four different flow rates (30, 50, 100, and 150 mL min^{-1} and current densities up to 6 A cm^{-2}). PTL2 was chosen for this analysis and the PTL parameters were set corresponding to PTL2 from Table 2.

Irrespective of the capillary pressure equation used (LE or BCE), the same trends were observed in the change to the saturation and anode overpotential with the current density and inlet flow rate. An increase in the current density leads to a decrease in the liquid saturation and an increase in the anode overpotential (Figures 3A and 4). On the other hand, an increase in the water flow rate showed an increase in the liquid saturation and a decrease in the anode overpotential (Figures 3B and 4). However, it is notable that the BCE simulations give a lower liquid saturation through the PTL thickness and higher mass transport overpotential compared to the LE simulation. These observations can be explained as follows.

At higher currents, more oxygen is produced, and thus more gas and less liquid are present in the pores of the PTL. The same trend was observed in the neutron imaging experiments in [6]: in a low water flow rate operation, the influence of the operating current density on the liquid saturation was significant. However, at a higher inlet flow rate, there is only a slight change in the liquid saturation. Additionally, the authors observed the existence of a critical current above which the gas saturation in the PTL is much higher. The model presented here also showed that at significantly high flow rates, the saturation profiles for different values of the current density come closer together—the saturation is less sensitive to the change in the current density for high inlet flow rates (Supplementary Information, Figure S1). However, no matter how much the flow rate is increased, the current density still had an influence on the saturation. This finding is in accordance with the experimental results in [8], where only an insignificant influence of the current density on the saturation was observed because the experiments were performed at a high inlet water flow rate. Furthermore, the existence of a critical current density was observed in this work in the same way as it was in the experimental study of Lee et al. [6]. Here, the critical current density corresponds to the current density above which the anode overpotential increases drastically (Figure 4). This is caused by the low liquid saturation at the ACL/PTL interface for the currents above critical. At a critical current density, the liquid saturation at the ACL/PTL interface dropped to a small value, approximately 0.2 (Figure 3A, red lines). Bearing in mind that the residual saturation was 0.1, it can be concluded that there is still some water on the surface of the ACL. However, only a small increase in the current density above the critical value decreases the saturation at the ACL/PTL interface further, leading to the ACL being completely covered with gas and thus to a reaction termination.

The increase in the inlet water flow rate leads to an increase in the PTL liquid saturation, as shown in Figure 3B. A better removal of the bubbles from the PTL and thus a lower accumulation of gas in the PTL and ACL at higher flow rates explains these results.

However, the beneficial influence of the flow rate was observed only up to a certain flow rate value. Once this value was reached, a further increase in the flow rate did not affect the liquid saturation, suggesting that there is an optimal value of the inlet flow rate. This trend was also observed in neutron imaging experiments [6,40]. Additionally, the literature suggests 100% liquid saturation at the AFC/PTL interface in most cases [8,24]. This is not realistic, because the bubble formation, growth, and detachment on the AFC/PTL interface are occurring continuously [41]. The experimental results from [8] showing 100% liquid saturation at the AFC/PTL interface could have been the consequence of the cell geometry and high water velocity. On the other hand, Lee et al. [6] found that the saturation at the AFC/PTL interface is dependent on the operating conditions. The model used in this study shows that the AFC/PTL saturation is dependent on the current density and inlet flow rate. This is a direct consequence of the boundary conditions at the AFC/PTL interface that correlate the gas/liquid conditions in the channel with the interface, and the boundary condition at the ACL/PTL interface that defines the fluxes based on the reaction rate. The AFC/PTL saturation increases with a decrease in the current density and an increase in the inlet flow rate, and it approaches one for a low current density and high flow rate (Supplementary Information, Figure S1).
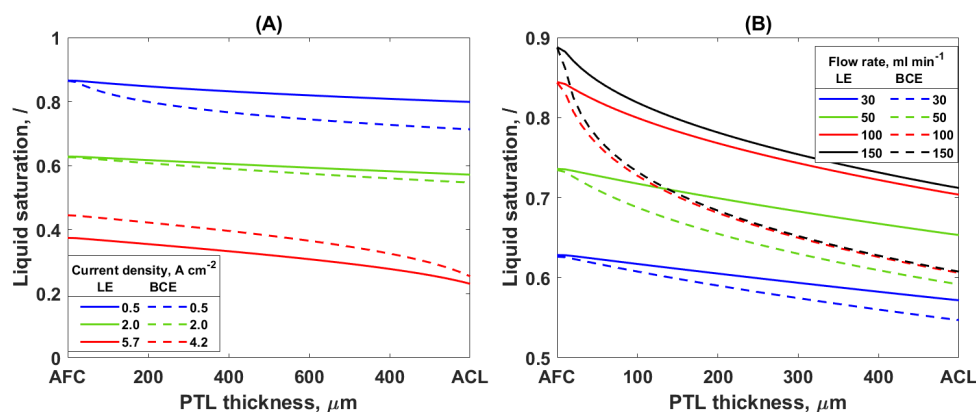

Figure 3. Liquid saturation through the PTL2 thickness (**A**) for different values of current density at inlet flow rate 30 mL min^{-1} and (**B**) for different values of inlet water flow rate at current density 2 A cm^{-2}; solid lines—LE simulation, dashed lines—BCE simulation.

Furthermore, it was proposed that there is a preferential pathway for the gas transport through the PTL [42–44]: with an increasing current density, the gas velocity through the PTL increases, but the pathway stays unaltered and the saturation profile through the PTL thickness does not change. The experimental results in [8,45] showed that the saturation profile has almost no sensitivity to the current density, supporting the assumption of the preferential gas pathway through the PTL. However, this was not shown in this work and partly contradicts the result in [6]. The reason for this difference might be explained by the high water flow rate used for the experiments in [8], or the different transport properties of the carbon paper PTL used in [45]. Additionally, the disagreement between the modeling results shown here and the experimental results in [6,8,45] can be attributed to the assumption of the lumped ACL which has different transport properties compared to the PTL. Recent works indicate that the contact between the catalyst layer and the PTL in the anode compartment contributes to the increase in the overpotential at high currents [12,14–16]. This could be taken into account by discretizing the ACL and introducing a potential distribution in the presented model.

Figure 4 shows the anode overpotential as a function of the current density for the different flow rates. The black line shows the activation overpotential, so the difference between the black line and colored line represents the mass transport contribution to the anode overpotential. Both the LE and BCE show similar trends and a relatively low mass transport overpotential, with higher values being obtained with the BCE simulations.

Considering that the mass transport overpotential is proportional to the liquid saturation, this result was expected. Both the activation and mass transport overpotentials increase with an increase in the current density, as has been reported previously [15]. At some point, when increasing the current density, the increase in the mass transport and anode overpotentials becomes exponential. This is the point at which the critical current density is observed. Furthermore, an increase in the flow rate allows for higher currents to be reached by increasing the critical current density. Furthermore, lower anode overpotentials are obtained when higher inlet water flow rates are used. As with the saturation, the beneficial influence of the inlet flow rate on the mass transport overpotential and critical current is present only up to a certain value of the flow rate. The optimal value of the flow rate depends on the operating current density: at higher current densities, a higher flow rate is needed. The experimental results in [6] show a small decrease in the mass transport overpotential with an increasing inlet flow rate, supporting the modeling results shown in this work. Additionally, Lickert et al. [7] investigated the influence of the flow fields on the electrolyzer performance. As in [6], they observed only a small change in the total potential due to the change in the inlet water flow rate. However, the mass transport overpotential was not determined from the experimental data. Additionally, for the electrolyzer operation without the flow fields, they observed a significant decrease in the cell voltage when the cell was operated at a higher inlet water flow rate.
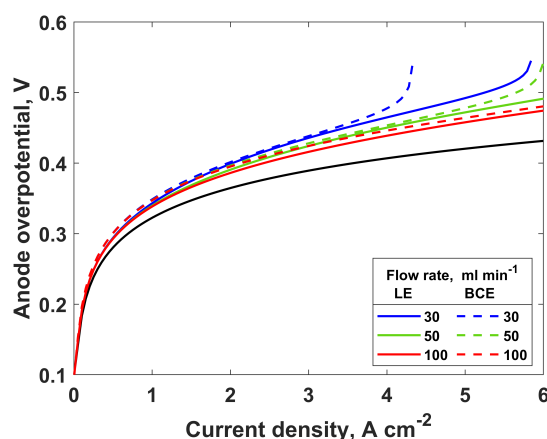
Figure 4. Anode overpotential as a function of current density for different inlet water flow rates for PTL2; solid lines—LE simulation, dashed lines—BCE simulation, black line—anode overpotential when there are no mass transport losses.

The mass transport overpotential calculated with this model ranges from a few mV at low currents up to approximately 100 mV at higher currents, which rather underestimates the mass transport overpotential obtained experimentally [10,15,16]. The higher mass transport overpotential obtained experimentally can indicate a mass transport resistance in the ACL, as well as in the catalyst layer and the GDL at the cathode side of the electrolyzer, which was not included in this model. Schmidt et al. [24] claim that the cathode mass transport overpotential is significant and even higher than the anode mass transport overpotential. This would explain why the model shows notably lower mass transport overpotential values compared to the experiments. Additionally, the discrepancy between the simulation and the experiments can be explained by the simple Tafel kinetics used to describe the oxygen evolution reaction. Many studies determined that the Tafel slope for the oxygen evolution reaction at the anode of the PEMWE is between 40 and 70 mV [4,15,16,46,47], indicating more complex oxygen evolution reaction kinetics. Furthermore, some suggest the Tafel slope changes with an increasing current density, causing the activation overpotential to bend toward higher values [46,48]. It is still not clear if this bending is due to a change in the reaction mechanism or to the mass transport resistances of the PEMWE. However, the change in the Tafel slope is not accounted for here. Based on

the definition of the mass transport overpotential in the present model, the higher the Tafel slope value, the higher the mass transport overpotential. Thus, a change in the Tafel slope with an increasing current density would result in a bigger mass transfer overpotential at higher currents. On the other hand, the application of the voltage breakdown methods based on the Tafel kinetics and high-frequency response can lead to the underestimation of the anode kinetic overpotential and an overestimation of the mass transport overpotential determined in the experimental studies.

Except for the current density and inlet flow rate, the model showed a high sensitivity to the conditions at the inlet. The value of the critical current density dropped significantly when a gas–liquid mixture was fed to the electrolyzer compared to the critical current density obtained for the liquid water feed (Supplementary Information, Figure S2). However, the model showed no dependency on the initial conditions in the channels or the PTL.

3.2. Influence of PTL Structure

The PTL structure and surface properties were found to have a determining effect on the mass transport losses of the electrolyzer [12,15,16]. Both the LE and BCE simulations were carried out in order to study the influence of the PTL structure on the PEMWE performance. The effect of the PTL structure was studied for five different PTLs which were analyzed experimentally in [16,39]. PTL1 was a sintered powder titanium with the lowest porosity, while PTL2-5 were fibrous titanium materials. PTL2 and PTL5 have the same fiber diameter but different porosities, pore sizes, PSDs, and consequentially absolute permeabilities and tortuosities. On the other hand, PTL2-4 have approximately the same porosity but different fiber diameters that caused differences in the pore sizes, PSDs, and absolute permeabilities of these structures. All the PTL parameters can be found in Table 2.

It was found that the PTL structure does not influence the liquid saturation at the AFC/PTL interface but the saturation in the bulk of the PTL, and especially at the ACL/PTL interface (Supplementary Information, Figure S3), which is also assumed to be the source of the mass transport losses in this model. Figure 5 shows the mass transport losses as a function of the current density obtained with the LE and BCE simulations for the different PTLs, as well as the experimental results from [15,16]. The modeling results predicted that PTL4 and PTL5 would outperform PTL1-3, having a lower mass transport overpotential and a higher saturation at the ACL/PTL interface. These two PTLs have a higher permeability and larger pores compared to the rest, which leads to better water and oxygen transport. The same was observed with both the LE and BCE simulations; however, the BCE simulations (Figure 5B, blue lines) showed a higher sensitivity to the PTL parameters compared to the LE simulations (Figure 5A, blue lines), as well as lower saturations and higher mass transport overpotentials. The maximum difference in the overpotentials due to the different PTLs was approximately 10 mV. The difference in the mass transport overpotentials of the different PTLs gradually increased with the current density in the LE simulations. On the other hand, the BCE simulations showed that the difference in the mass transport overpotentials for the different PTLs was almost independent of the current density, with exceptions for the low current densities and currents near the limiting current density. If we compare all the PTLs, the sintered PTL had the worst performance due to its low porosity and the small pores that result in a low permeability. From the fibrous PTLs, the highest mass transport overpotential was obtained for PTL2, followed by PTL3. Both PTL2 and PTL3 had a significantly lower absolute permeability compared to PTL4 and PTL5 which showed the lowest mass transport overpotentials and highest ACL/PTL interface saturations. Additionally, PTL2 is made of the thinnest fibers and has the smallest pores of all fibrous PTLs. This is the reason for the high overpotential determined in the simulations for PTL2. Furthermore, PTL4 and PTL5 showed the same performance even though their structures are different. However, the absolute permeabilities of these two materials were similar and much higher compared to PTL1-3. Based on this, one can assume that this model is highly sensitive to the value of absolute permeability.

Furthermore, this analysis showed that a higher porosity and bigger pores would lead to better oxygen removal from the catalyst layer (higher absolute permeability of the porous structure) and the lower mass transport losses. The same effect was present for the wider PSD (lower PSD index values) of the PTL. Even though porosity is a parameter that is frequently used to describe the macroscopic structure of the PTL, it is also necessary to take into account the pore sizes of the PTL, because the transport properties of the PTL will differ depending on the internal PTL structure. This is taken into account directly with the BCE for the capillary pressure via two parameters: the maximum pore radius and PSD index. On the other hand, the LE capillary pressure takes the structure into account indirectly through the bulk parameter, porosity, as well as the absolute permeability value.
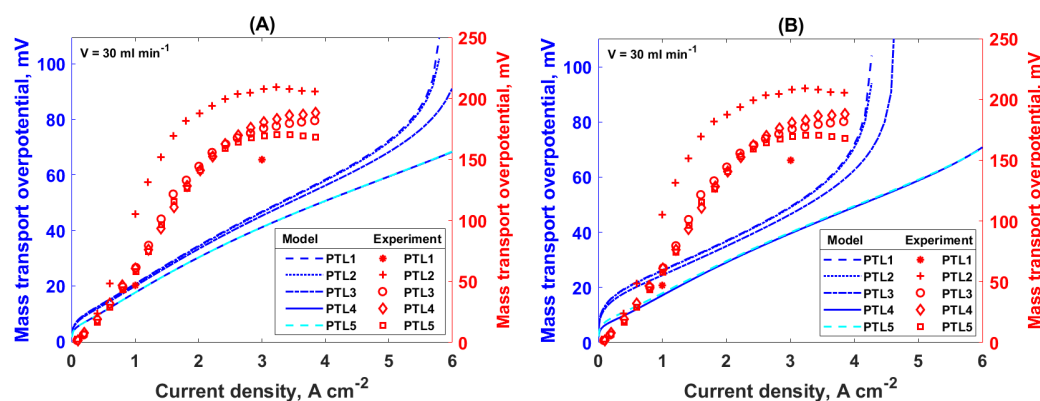
Figure 5. Mass transport overpotential as a function of current density for different PTLs at an inlet flow rate of 30 mL min^{-1} obtained with (**A**) LE and (**B**) BCE simulations; lines—model results, symbols—experimental results adopted from [15,16].

Experimentally, it was shown that PTL5 has the lowest mass transport overpotential due to the high porosity and high permeability. This is followed by PTL4, PTL3, and PTL2 at lower current densities, while at higher current densities, PTL3 performed better than PTL4 (Figure 5, red symbols) [16]. The model is capable of reproducing the general dependency of the mass transport overpotential at lower current densities on the PTL structure that was observed experimentally in [16]. However, in contradiction to the simulations which show an exponential increase in the mass transport overpotential at high current densities, the experimental data show that the mass transport overpotential saturates at higher current densities. A slight decrease in the mass transport overpotential at high currents is even observed for PTL2 and PTL5, and no PTL has shown a limiting current behavior (a sudden increase in the mass transport overpotential). The plateau and decrease in the mass transport overpotential at high currents observed in [16] can be explained by the nonisothermal conditions during the experiments for the current densities above approximately 1.5 A cm^{-2}. Because the mathematical model is isothermal, we limit the comparison of the experiment and model to the low current density region. In this region, there is a qualitative agreement between the experimental and modeling results. Additionally, the model predictions qualitatively agree with the experimental results in [6], where the mass transport overpotential increased with the current density until the limiting current density was reached. Nevertheless, quantitatively, there is an underestimation of the mass transport overpotential calculated with the model compared to the one determined experimentally in the literature [6,15,16]. As already discussed in Section 3.1, this discrepancy can be explained by the method based on the Tafel kinetics used for determining the mass transport overpotential from the experimental data, as well as with the model assumptions (no mass transport overpotential caused by the mass transport in the GDL and the catalyst layers). Moreover, it should be borne in mind that the model used in this study was not fitted to the experimental data. Additionally, the model shows a steep increase in the mass transport overpotential at low current densities, contrary to the experimentally determined mass transport overpotential. The main assumption

for the experimental determination of the mass transport overpotential is that the mass transport overpotential at low current densities is negligible and, usually, only the kinetic and ohmic overpotential contributions are taken into account in the region between 10 and 100 mA cm^{-2}. The modeling results shown here indicate that this assumption is not appropriate and that the mass transport overpotential contributes to the overall potential losses of the PEMWE, even at the low current densities.

PTL1 showed the worst performance in this study. Experimentally, PTL1 was analyzed in [15], and it showed quite a good performance, better than all the fibrous PTLs studied in [16]. However, because PTL1 was analyzed in a separate study, a comparison of the experimental results obtained for PTL1 with the results obtained for the fibrous PTLs is not meaningful and a disagreement with the model predictions for PTL1 was expected.

Lastly, the influence of the PTL thickness was investigated, and the results are presented in Figure 6. As expected, the thinner PTL resulted in a higher saturation at the ACL and a lower mass transport overpotential. However, the AFC/PTL saturation was not affected by the PTL thickness. Considering that in the thinner PTL the gas and water need to travel a shorter distance, the gas removal and water supply are easier and faster, indicating that the cell voltage would be lower for the thinner PTL. This was shown experimentally in [15] by comparing the performance of two PTLs of the same structure but different thicknesses: 1 and 2 mm. The determined mass transport resistance was smaller for the thinner PTL.
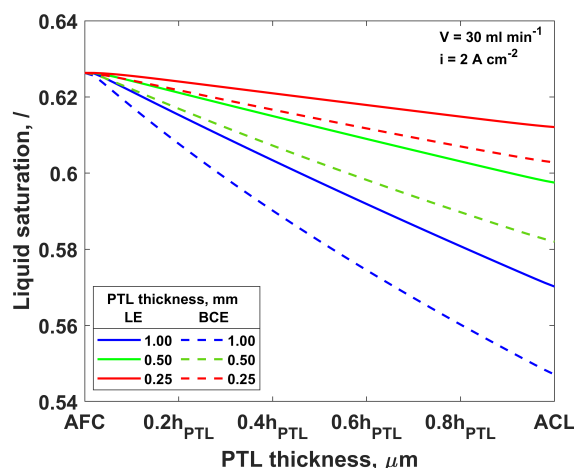
Figure 6. Liquid saturation through PTL2 thickness for different total thicknesses of the PTL2 at inlet flow rate 30 mL min^{-1} and current density 2 A cm^{-2}; solid lines—LE simulation, dashed lines—BCE simulation.

3.3. PTL with Gradient

In the polymer electrolyte membrane fuel cells (PEMFC), as a more mature technology than the PEMWE, the MPL is usually sandwiched between the catalyst layer and the GDL. This MPL allows for better contact between the catalyst and GDL, as well as a supply of the reactants. Because much knowledge obtained from the PEMFC can be transferred and applied to the PEMWE, the use of the MPL in the anode compartment of the electrolyzer was investigated. Schuler et al. [17] compared the PEMWE performance with and without the MPL. They found out that the MPL results in a decrease in the cell voltage due to the better contact between the ACL and MPL. Lettenmeier et al. [35] produced a PTL with a gradient in the pore size distribution along the thickness. The electrochemical tests of the novel PTL in the PEMWEs showed a decrease in the mass transport limitations compared to the mesh PTLs, which was attributed to the pore size gradient of the PTL. Additionally, the pore network model analysis indicated that the optimal design of the PTL for the removal of gas from the electrode is a low-to-high (LTH) through-thickness gradient in the direction from the ACL to the AFC [6,42].

Both the LTH and high-to-low (HTL) gradients were analyzed in this study. The structural parameters of the graded PTLs are shown in Table 3. The HTL gradient was the same as the LTH gradient, but in the opposite direction: the largest porosity and pores were on the side of the PTL facing the ACL, while the smallest porosity and pores were facing the AFC. The LE simulations showed a small positive effect of both the LTH and HTL gradients on the liquid saturation through the PTL (Figure 7, solid lines) compared to the uniform PTL (PTL2). This is probably caused by the higher absolute permeability of the graded PTL and the higher total volume of the pores. On the other hand, the BCE simulations showed that the gradient in the pore size and porosity influences the PTL saturation (Figure 7, dashed lines). Interestingly, the LTH gradient resulted in a significant increase in the liquid saturation near the ACL and a decrease in the mass transport losses, while the HTL-graded PTL showed a decrease in the liquid saturation and PEMWE performance compared to PTL2. Based on the BCE simulations, the smaller pores in the PTL contain water and the larger pores are filled with gas. Having an MPL between the PTL and ACL would lead to the easier removal of gas and the better retention of water near the ACL, thus decreasing the mass transport losses. Even though the experimental studies showed a performance improvement with the graded PTLs [17,35], the observed improvement was not attributed to a decrease in the mass transport resistance due to the improved two-phase transport in the PTL but to the lower contact resistance between the PTL and ACL. This model shows that the two-phase transport would also be ameliorated in the graded PTL compared to the uniform one.

Table 3. Graded PTL parameters.

Parameter	LTH Graded PTL	HTL Graded PTL
Porosity, ε, %	55(ACL)—75(AFC)	75(ACL)—55(AFC)
Maximum pore radius, r_{max}, μm	35(ACL)—50(AFC)	50(ACL)—35(AFC)
Tortuosity, τ, /	1.4	1.4
Absolute permeability. m^2	1.1×10^{-11}	1.1×10^{-11}
PSD index, λ, /	1.75	1.75
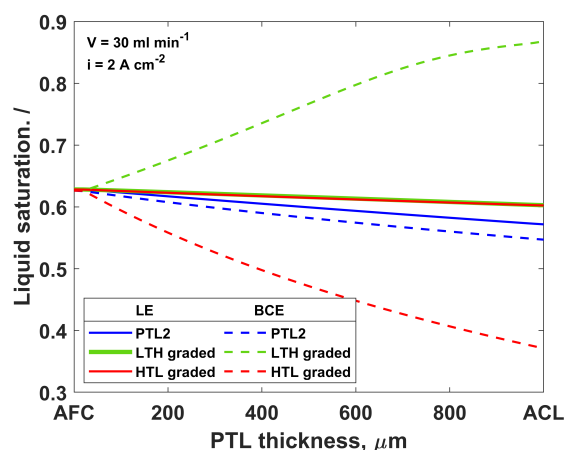
Figure 7. Liquid saturation through PTL thickness for graded and uniform PTLs at inlet flow rate 30 mL min^{-1} and current density 2 A cm^{-2}; solid lines—LE simulation, dashed lines—BCE simulation.

4. Conclusions

In this work, a nonlinear dynamic macroscopic model coupling the mass transport and the electrochemical reaction was developed to analyze the performance of the PEMWE. The influences of the operating conditions and PTL structure were discussed.

It was found that both the current density and inlet water flow rate influence the mass transport losses of the electrolyzer. A current density increase leads to a higher gas

accumulation in the PTL and an increase in the overpotential, while an increase in the water flow rate has the opposite effect. A critical current density at which almost the whole catalyst layer is covered with gas and no reaction occurs was observed. The value of the critical current density can be shifted to higher values by increasing the inlet water flow rate. Additionally, an optimal flow rate exists as a plateau in the overpotential is reached when the flow rate is increased. The value of the optimal inlet flow rate is dependent on the current density, and it increases with the current density. The PTL structural properties were shown to influence the mass transport overpotential and critical current density: a high porosity, wide PSD, and large pores showed beneficial effects. Furthermore, two capillary pressure correlations were compared for the simulations of the two-phase flow in the PTL: the Leverette and Brooks–Corey equations. Overall, the Brooks–Corey equation simulations showed a better agreement with the literature findings.

Though the presented model was able to qualitatively reproduce the behavior of the PEMWE, further developments would lead to more precise results and a better understanding of the mass transport losses. One of the major tasks is to describe the two-phase transport through the PTL, as well as the contact between the catalyst layer and the PTL. To do this, a more appropriate capillary pressure equation is required, as well as a more authentic definition of both the catalyst layer and the PTL structures and their influence on the electrolyzer performance. However, as shown in this work, macroscopic models are invaluable for analyzing the PEMWE behavior because they can predict the influence of the operating and design parameters on the performance at low computational costs. Furthermore, macroscopic mathematical models permit a more detailed and more precise interpretation of the experimental results compared to the fast voltage breakdown methods that are usually used.

List of Symbols

A_p, B_p, C_p	constants in Antoine equation for the vapor pressure of water; /
C	molar concentration, mol m^{-3}
C_{dl}	double-layer capacitance, F m^{-2}
D_{eff}	effective diffusivity in oxygen–vapor mixture, m^2 s^{-1}
D_W	diffusion coefficient of water through the membrane, m^2 s^{-1}
ΔG	change in free Gibbs energy, J mol^{-1}
E_{cell}	electrolyzer potential, V
E_{ocv}	open-circuit electrolyzer potential, V
F	Faraday's constant, C mol^{-1}
h	thickness, m
j	current density, A m^{-2}
j_0	exchange current density, A m^{-2}
k_r	relative permeability, /
k_W	water evaporation/condensation rate constant, s^{-1}
K	absolute permeability of porous media, m^2 s^{-1}
l	flow channel length, m
M	molar mass, kg mol^{-1}
n_{eod}	electro-osmotic drag coefficient, /
N	volumetric flow rate, mol m^{-3} s^{-1}
p	pressure, Pa
p_c	capillary pressure, Pa
$p_{H_2O}^{sat}$	vapor pressure, Pa
r	reaction rate, mol m^{-2} s^{-1}
r_{max}	maximum pore radius, m
R_W	water–phase–change volumetric flow rate, mol m^{-3} s^{-1}
R	universal gas constant, J mol^{-1} K^{-1}
s	phase saturation, /
S	normalized liquid saturation, /
t	time, s
T	temperature, K
u	velocity, m s^{-1}
U	velocity, m s^{-1}
y	molar fraction in gas phase, /
z	sandwich coordinate, m
α	charge transfer coefficient, /
γ	contact angle, rad
ε	porosity, /
ϵ	gas volume fraction at the flow channels, /
θ	bubble coverage, /
κ	specific conductivity, S m^{-1}
λ_{mem}	membrane humidity, /
λ	pore size distribution index, /
μ	viscosity, Pa s
ρ	density, kg m^{-3}
σ	surface tension, N m^{-1}
τ	tortuosity, /

Superscripts

ACL	anode catalyst layer
AFC	anode flow channel
C	cathode
diff	diffusion
eod	electro osmotic drag
mem	membrane
PTL	porous transport layer

Subscripts

A　　　　　　anode
C　　　　　　cathode
i　　　　　　species: $H_2(g)$, $O_2(g)$, $H_2O(l)$, $H_2O(g)$, $N_2(g)$
k　　　　　　aggregate state: *g*—gas phase, *l*—liquid phase
r　　　　　　residual
0　　　　　　initial value

Abbreviations

ACL　　　　　anode catalyst layer
AFC　　　　　anode flow channel
BCE　　　　　Brooks–Corey equation
C　　　　　　cathode
CCL　　　　　cathode catalyst layer
DAE　　　　　differential-algebraic equations
GDL　　　　　gas diffusion layer
HTL　　　　　high to low
LE　　　　　Leverette equation
LTH　　　　　low to high
MEA　　　　　membrane electrode assembly
MEM　　　　　membrane
MPL　　　　　microporous layer
PEMFC　　　　proton exchange membrane fuel cell
PEMWE　　　proton exchange membrane water electrolyzer
PNM　　　　　pore network model
PSD　　　　　pore size distribution
PTL　　　　　porous transport layer

References

1.　Ayers, K.; Danilovic, N.; Ouimet, R.; Carmo, M.; Pivovar, B.; Bornstein, M. Perspectives on Low-Temperature Electrolysis and Potential for Renewable Hydrogen at Scale. *Annu. Rev. Chem. Biomol. Eng.* **2019**, *10*, 219–239. [CrossRef]
2.　Fonseca, J.D.; Camargo, M.; Commenge, J.M.; Falk, L.; Gil, I.D. Trends in design of distributed energy systems using hydrogen as energy vector: A systematic literature review. *Int. J. Hydrogen Energy* **2019**, *44*, 9486–9504. [CrossRef]
3.　Millet, P.; Grigoriev, S. Chapter 2—Water Electrolysis Technologies. In *Renewable Hydrogen Technologies*; Gandía, L.M., Arzamendi, G., Diéguez, P.M., Eds.; Elsevier: Amsterdam, The Netherlands, 2013; pp. 19–41. [CrossRef]
4.　Babic, U.; Suermann, M.; Büchi, F.N.; Gubler, L.; Schmidt, T.J. Critical Review—Identifying Critical Gaps for Polymer Electrolyte Water Electrolysis Development. *J. Electrochem. Soc.* **2017**, *164*, F387–F399. [CrossRef]
5.　Carmo, M.; Fritz, D.L.; Mergel, J.; Stolten, D. A comprehensive review on PEM water electrolysis. *Int. J. Hydrogen Energy* **2013**, *38*, 4901–4934. [CrossRef]
6.　Lee, J.K.; Lee, C.; Fahy, K.F.; Zhao, B.; LaManna, J.M.; Baltic, E.; Jacobson, D.L.; Hussey, D.S.; Bazylak, A. Critical Current Density as a Performance Indicator for Gas-Evolving Electrochemical Devices. *Cell Rep. Phys. Sci.* **2020**, *1*, 100147. [CrossRef]
7.　Lickert, T.; Kiermaier, M.L.; Bromberger, K.; Ghinaiya, J.; Metz, S.; Fallisch, A.; Smolinka, T. On the influence of the anodic porous transport layer on PEM electrolysis performance at high current densities. *Int. J. Hydrogen Energy* **2020**, *45*, 6047–6058. [CrossRef]
8.　Zlobinski, M.; Schuler, T.; Büchi, F.N.; Schmidt, T.J.; Boillat, P. Transient and Steady State Two-Phase Flow in Anodic Porous Transport Layer of Proton Exchange Membrane Water Electrolyzer. *J. Electrochem. Soc.* **2020**, *167*, 084509. [CrossRef]
9.　Garcia-Navarro, J.C.; Schulze, M.; Friedrich, K.A. Measuring and modeling mass transport losses in proton exchange membrane water electrolyzers using electrochemical impedance spectroscopy. *J. Power Sources* **2019**, *431*, 189–204. [CrossRef]
10.　Peng, X.; Satjaritanun, P.; Taie, Z.; Wiles, L.; Keane, A.; Capuano, C.; Zenyuk, I.V.; Danilovic, N. Insights into Interfacial and Bulk Transport Phenomena Affecting Proton Exchange Membrane Water Electrolyzer Performance at Ultra-Low Iridium Loadings. *Adv. Sci.* **2021**, *8*, 2102950. [CrossRef]
11.　Grigoriev, S.A.; Millet, P.; Volobuev, S.A.; Fateev, V.N. Optimization of porous current collectors for PEM water electrolysers. *Int. J. Hydrogen Energy* **2009**, *34*, 4968–4973. [CrossRef]
12.　Majasan, J.O.; Iacoviello, F.; Cho, J.I.S.; Maier, M.; Lu, X.; Neville, T.P.; Dedigama, I.; Shearing, P.R.; Brett, D.J.L. Correlative study of microstructure and performance for porous transport layers in polymer electrolyte membrane water electrolysers by X-ray computed tomography and electrochemical characterization. *Int. J. Hydrogen Energy* **2019**, *44*, 19519–19532. [CrossRef]
13.　Pushkarev, A.S.; Pushkareva, I.V.; Solovyev, M.A.; Prokop, M.; Bystron, T.; Rajagopalan, S.K.; Bouzek, K.; Grigoriev, S.A. On the influence of porous transport layers parameters on the performances of polymer electrolyte membrane water electrolysis cells. *Electrochim. Acta* **2021**, *399*, 139436. [CrossRef]

14. Lopata, J.; Kang, Z.; Young, J.; Bender, G.; Weidner, J.W.; Shimpalee, S. Effects of the Transport/Catalyst Layer Interface and Catalyst Loading on Mass and Charge Transport Phenomena in Polymer Electrolyte Membrane Water Electrolysis Devices. *J. Electrochem. Soc.* **2020**, *167*, 064507. [CrossRef]
15. Suermann, M.; Takanohashi, K.; Lamibrac, A.; Schmidt, T.J.; Büchi, F.N. Influence of Operating Conditions and Material Properties on the Mass Transport Losses of Polymer Electrolyte Water Electrolysis. *J. Electrochem. Soc.* **2017**, *164*, F973–F980. [CrossRef]
16. Schuler, T.; Schmidt, T.J.; Büchi, F.N. Polymer Electrolyte Water Electrolysis: Correlating Performance and Porous Transport Layer Structure: Part II. Electrochemical Performance Analysis. *J. Electrochem. Soc.* **2019**, *166*, F555–F565. [CrossRef]
17. Schuler, T.; Ciccone, J.; Krentscher, B.; Marone, F.; Peter, C.; Schmidt, T.; Büchi, F. Hierarchically Structured Porous Transport Layers for Polymer Electrolyte Water Electrolysis. *Adv. Energy Mater.* **2019**, *10*, 1903216. [CrossRef]
18. Zlobinski, M.; Schuler, T.; Büchi, F.N.; Schmidt, T.J.; Boillat, P. Elucidation of Fluid Streamlining in Multi-Layered Porous Transport Layers for Polymer Electrolyte Water Electrolyzers by Operando Neutron Radiography. *J. Electrochem. Soc.* **2021**, *168*, 014505. [CrossRef]
19. Mo, J.; Kang, Z.; Yang, G.; Retterer, S.T.; Cullen, D.A.; Toops, T.J.; Green, J.B.; Zhang, F.Y. Thin liquid/gas diffusion layers for high-efficiency hydrogen production from water splitting. *Appl. Energy* **2016**, *177*, 817–822. [CrossRef]
20. Kang, Z.; Mo, J.; Yang, G.; Li, Y.; Talley, D.A.; Retterer, S.T.; Cullen, D.A.; Toops, T.J.; Brady, M.P.; Bender, G.; et al. Thin film surface modifications of thin/tunable liquid/gas diffusion layers for high-efficiency proton exchange membrane electrolyzer cells. *Appl. Energy* **2017**, *206*, 983–990. [CrossRef]
21. Kang, Z.; Yang, G.; Mo, J.; Yu, S.; Cullen, D.A.; Retterer, S.T.; Toops, T.J.; Brady, M.P.; Bender, G.; Pivovar, B.S.; et al. Developing titanium micro/nano porous layers on planar thin/tunable LGDLs for high-efficiency hydrogen production. *Int. J. Hydrogen Energy* **2018**, *43*, 14618–14628. [CrossRef]
22. Kim, P.J.; Lee, C.H.; Lee, J.K.; Fahy, K.F.; Bazylak, A. In-Plane Transport in Water Electrolyzer Porous Transport Layers with Through Pores. *J. Electrochem. Soc.* **2020**, *167*, 124522. [CrossRef]
23. Falcão, D.S.; Pinto, A.M.F.R. A review on PEM electrolyzer modelling: Guidelines for beginners. *J. Clean. Prod.* **2020**, *261*, 121184. [CrossRef]
24. Schmidt, G.; Suermann, M.; Bensmann, B.; Hanke-Rauschenbach, R.; Neuweiler, I. Modeling Overpotentials Related to Mass Transport Through Porous Transport Layers of PEM Water Electrolysis Cells. *J. Electrochem. Soc.* **2020**, *167*, 114511. [CrossRef]
25. Kim, H.; Park, M.; Lee, K.S. One-dimensional dynamic modeling of a high-pressure water electrolysis system for hydrogen production. *Int. J. Hydrogen Energy* **2013**, *38*, 2596–2609. [CrossRef]
26. Han, B.; Mo, J.; Kang, Z.; Yang, G.; Barnhill, W.; Zhang, F.Y. Modeling of two-phase transport in proton exchange membrane electrolyzer cells for hydrogen energy. *Int. J. Hydrogen Energy* **2017**, *42*, 4478–4489. [CrossRef]
27. García-Salaberri, P.A. 1D two-phase, non-isothermal modeling of a proton exchange membrane water electrolyzer: An optimization perspective. *J. Power Sources* **2022**, *521*, 230915. [CrossRef]
28. Wrubel, J.A.; Kang, Z.; Witteman, L.; Zhang, F.Y.; Ma, Z.; Bender, G. Mathematical modeling of novel porous transport layer architectures for proton exchange membrane electrolysis cells. *Int. J. Hydrogen Energy* **2021**, *46*, 25341–25354. [CrossRef]
29. Don, W.G.; Robert, H.P. *Perry's Chemical Engineers' Handbook*, 8th ed.; McGraw-Hill Education: New York, NY, USA, 2008.
30. Starikovičius, V. *The Multiphase Flow and Heat Transfer in Porous Media*; Report, Fraunhofer Institut Techno- und Wirtschaftsmathematik ITWM: Kaiserslautern, Germany, 2003.
31. Grigoriev, S.A.; Kalinnikov, A.A.; Millet, P.; Porembsky, V.I.; Fateev, V.N. Mathematical modeling of high-pressure PEM water electrolysis. *J. Appl. Electrochem.* **2010**, *40*, 921–932. [CrossRef]
32. Brooks, R.H.; Corey, A.T. Hydraulic Properties of Porous Media and Their Relation to Drainage Design. *Trans. ASAE* **1964**, *7*, 0026–0028. [CrossRef]
33. Rajora, A.; Haverkort, J.W. An Analytical Model for Liquid and Gas Diffusion Layers in Electrolyzers and Fuel Cells. *J. Electrochem. Soc.* **2021**, *168*, 034506. [CrossRef]
34. Altaf, H.; Vorhauer, N.; Tsotsas, E.; Vidaković-Koch, T. Steady-State Water Drainage by Oxygen in Anodic Porous Transport Layer of Electrolyzers: A 2D Pore Network Study. *Processes* **2020**, *8*, 362. [CrossRef]
35. Lettenmeier, P.; Kolb, S.; Sata, N.; Fallisch, A.; Zielke, L.; Thiele, S.; Gago, A.S.; Friedrich, K.A. Comprehensive investigation of novel pore-graded gas diffusion layers for high-performance and cost-effective proton exchange membrane electrolyzers. *Energy Environ. Sci.* **2017**, *10*, 2521–2533. [CrossRef]
36. Stiber, S.; Balzer, H.; Wierhake, A.; Wirkert, F.J.; Roth, J.; Rost, U.; Brodmann, M.; Lee, J.K.; Bazylak, A.; Waiblinger, W.; et al. Porous Transport Layers for Proton Exchange Membrane Electrolysis Under Extreme Conditions of Current Density, Temperature, and Pressure. *Adv. Energy Mater.* **2021**, *11*, 2100630. [CrossRef]
37. Marangio, F.; Santarelli, M.; Calì, M. Theoretical model and experimental analysis of a high pressure PEM water electrolyser for hydrogen production. *Int. J. Hydrogen Energy* **2009**, *34*, 1143–1158. [CrossRef]
38. Ma, Z.; Zhang, Y.; Liu, S.; Xu, W.; Wu, L.; Hsieh, Y.C.; Liu, P.; Zhu, Y.; Sasaki, K.; Renner, J.N.; et al. Reaction mechanism for oxygen evolution on RuO2, IrO2, and RuO2@IrO2 core-shell nanocatalysts. *J. Electroanal. Chem.* **2018**, *819*, 296–305. [CrossRef]
39. Schuler, T.; De Bruycker, R.; Schmidt, T.J.; Büchi, F.N. Polymer Electrolyte Water Electrolysis: Correlating Porous Transport Layer Structural Properties and Performance: Part I. Tomographic Analysis of Morphology and Topology. *J. Electrochem. Soc.* **2019**, *166*, F270–F281. [CrossRef]

40. Selamet, O.F.; Pasaogullari, U.; Spernjak, D.; Hussey, D.S.; Jacobson, D.L.; Mat, M.D. Two-phase flow in a proton exchange membrane electrolyzer visualized in situ by simultaneous neutron radiography and optical imaging. *Int. J. Hydrogen Energy* **2013**, *38*, 5823–5835. [CrossRef]

41. Hoeh, M.A.; Arlt, T.; Manke, I.; Banhart, J.; Fritz, D.L.; Maier, W.; Lehnert, W. In operando synchrotron X-ray radiography studies of polymer electrolyte membrane water electrolyzers. *Electrochem. Commun.* **2015**, *55*, 55–59. [CrossRef]

42. Vorhauer-Huget, N.; Altaf, H.; Dürr, R.; Tsotsas, E.; Vidaković-Koch, T. Computational Optimization of Porous Structures for Electrochemical Processes. *Processes* **2020**, *8*, 1205. [CrossRef]

43. Lee, J.K.; Lee, C.H.; Bazylak, A. Pore network modelling to enhance liquid water transport through porous transport layers for polymer electrolyte membrane electrolyzers. *J. Power Sources* **2019**, *437*, 226910. [CrossRef]

44. Panchenko, U.; Giesenberg, L.; Borgardt, E.; Zwaygardt, W.; Kardjilov, N.; Markötter, H.; Arlt, T.; Manke, I.; Müller, M.; Stolten, D.; et al. Influence of Stoichiometry on the Two-Phase Flow Behavior of Proton Exchange Membrane Electrolyzers. *Energies* **2019**, *12*, 350. [CrossRef]

45. Satjaritanun, P.; O'Brien, M.; Kulkarni, D.; Shimpalee, S.; Capuano, C.; Ayers, K.E.; Danilovic, N.; Parkinson, D.Y.; Zenyuk, I.V. Observation of Preferential Pathways for Oxygen Removal through Porous Transport Layers of Polymer Electrolyte Water Electrolyzers. *iScience* **2020**, *23*, 101783. [CrossRef] [PubMed]

46. Papakonstantinou, G.; Algara-Siller, G.; Teschner, D.; Vidaković-Koch, T.; Schlögl, R.; Sundmacher, K. Degradation study of a proton exchange membrane water electrolyzer under dynamic operation conditions. *Appl. Energy* **2020**, *280*, 115911. [CrossRef]

47. Bernt, M.; Siebel, A.; Gasteiger, H.A. Analysis of Voltage Losses in PEM Water Electrolyzers with Low Platinum Group Metal Loadings. *J. Electrochem. Soc.* **2018**, *165*, F305–F314. [CrossRef]

48. Nong, H.N.; Falling, L.J.; Bergmann, A.; Klingenhof, M.; Tran, H.P.; Spöri, C.; Mom, R.; Timoshenko, J.; Zichittella, G.; Knop-Gericke, A.; et al. Key role of chemistry versus bias in electrocatalytic oxygen evolution. *Nature* **2020**, *587*, 408–413. [CrossRef] [PubMed]